Rock and Soil Mechanics 2024 45(4): 991−1002
https: //doi.org/10.26599/RSM.2024.9435614
ISSN 1000−7598
journal homepage: rocksoilmech.whrsm.ac.cn

# Energy attenuation patterns of microseismic signals in the "three zones" of goaf based on variational mode decomposition

JIA Bao-xin[1, 2], ZHENG Ke-nan[1], ZHOU Lin-li[1]

(1. School of Civil Engineering, Liaoning Technical University, Fuxin, Liaoning 123000, China;
2. Liaoning Key Laboratory of Mine Subsidence Disaster Prevention and Control, Liaoning Technical University, Fuxin, Liaoning 123000, China)

**Abstract:** In order to investigate the energy attenuation of microseismic signal in the "three-zone" structure of goaf, a similar model test of the overburden of goaf is proposed to collect the artificially excited microseismic signals propagated through the structure of goaf. The relationship between the central frequency and energy of the mode components of the microseismic signal via variational mode decomposition (VMD) is analysed. The optimal number of mode components of the microseismic signal is determined according to the central frequency method, and the energy of each component is calculated for the under-decomposition, optimal decomposition and over-decomposition states of the microseismic signal. The relationship between the energy of each mode component and the central frequency distribution is fitted for the optimal decomposition state of the signal under each source, and the energy of each mode component is analysed for different propagation states of the microseismic signal in the "three-zone" structure. The effect of each structural layer on the energy of the microseismic signal under different propagation states of the "three-zone" structure is analyzed. The results of the study show that: (1) The number of effective modes of the artificially excited vibration signal in the VMD process ranges from 6 to 11, and the energy of the microseismic signal varies significantly with the number of modes. (2) The power function can be used to fit the mode energy versus frequency of the microseismic signal, and the fitting state is good (the coefficient of determination is greater than 0.9), in which the low-frequency mode component contains nearly 50% of the total energy of the signal. The Gaussian function can be used to fit the distribution performance of the energy of each component of the source in the frequency domain, and the fitting state is good and shows the Gaussian single-peak characteristic. (3) The microseismic signal traverses through the "three-zone" structure of goaf, and the energy of the microseismic signal decreases as the distance between the source location and the sensor increases. The collapse zone has a significant attenuating effect on the signal compared to the fracture zone and the bending zone. The energy of the microseismic signal does not change as it passes through the "three-zone" structure of goaf.

**Keywords:** variational mode decomposition (VMD); microseismic signal; signal frequency characteristics; signal energy attenuation; three-zone structure of goaf

## 1 Introduction

With the advancement of coal mine production activities, the original coal-bearing sedimentary strata are mined out, leading to the formation of the "three-zone" structure of the goaf. In the process of microseismic monitoring, it is essential to consider the influence of the complex geological structure of the mine on the propagation of microseismic waves. The microseismic signals contain a wealth of geological information, among which the energy of microseismic signals is considered as an important parameter to describe the propagation state of microseismic waves. Therefore, investigating the attenuation characteristics of microseismic signals within the "three-zone" structure of the goaf can provide a reference to determine the activity patterns of potential dynamic disasters, which is of great significance for the study of microseismic monitoring in mines.

The microseismic signals primarily include rock rupture signals, coal mine blast signals, mechanical vibration signals, and other construction noise signals[1]. The presence of noise signals can affect the calculation of microseismic signal energy. However, accurate calculation of microseismic signal energy is the key to the research on microseismic signal energy. Therefore, the reasonable extraction of the effective components of the microseismic signal for signal energy calculation is a crucial prerequisite to ensuring the accuracy and effectiveness of microseismic monitoring in coal mines. At present, adaptive signal decomposition methods, such as empirical mode decomposition (EMD)[2−3] and empirical wavelet transform (EWT)[4], can achieve signal decomposition and noise filtering. However, the use of EMD for signal decomposition is prone to induce the issues such as mode aliasing and endpoint effects[5], while the EWT is susceptible to the noise and uneven distribution of spectral amplitude, resulting in sparse and uneven spectral segmentation. Dragomiretskiy et al.[6] proposed the variational mode decomposition (VMD) based on EMD, which is a variational analysis

Received: 18 May 2023 Accepted: 4 September 2023
This work was supported by the General Program of National Natural Science Foundation of China (51774173) and the “Hundred, thousand, and ten thousand Talents Project” of Liaoning Province (2021921023).
First author: JIA Bao-xin, male, born in 1978, PhD, Professor, mainly engaged in research on mine disaster mechanics and underground engineering disaster prevention and mitigation. E-mail: jbx_811010@126.com
Corresponding author: ZHOU Lin-li, male, born in 1995, PhD, Lecturer, mainly engaged in research on geotechnical engineering and microseismic monitoring. E-mail：larryzll@163.com

method based on the frequency information of the signal. This approach has strong noise robustness[7], good self-adaptation, and solid mathematical foundation. However, an inappropriate number of mode components affects the signal decomposition results and has a significant influence on the signal analysis. The central frequency observation method[8–10], constructing indicators for optimization[11], and particle swarm algorithm[12–14] can be used to determine the reasonable number of mode components for VMD, thereby facilitating its application in signal noise reduction, feature extraction of vibration signals, and other related domains.

The microseismic signal energy is an important indicator of signal changes in the microseismic monitoring system. The change in energy can reflect the change characteristics of complex strata during the signal propagation process. In order to analyze the signal energy characteristics, Jia et al.[15] summarized the relationship between the instantaneous energy attenuation of microseismic signals in layered rock mass and the propagation distance, propagation velocity, and structural surface. Jia et al.[16] considered different propagation velocities of microseismic waves in different layered rocks, established the wavefront equation of microseismic waves, and summarized the microseismic signal propagation characteristics of the specific geological structures. Zhao et al.[17] derived the microseismic signal energy evolution characteristics during the loading process by conducting loading tests on fractured rocks, and elaborated the effect of fracture inclination angle on the signal energy. Martínez-Martínez et al.[18] proposed a spatial attenuation parameter that is sensitive to the petrographic characteristics and defects of the rock based on the energy of acoustic waves. Liu[19] applied fast Fourier transform and S-transform to obtain the amplitude-frequency and time-frequency characteristics of microseismic activity, and differentiated the types of rockburst by energy distribution characteristics. Liu et al.[20] studied the energy attenuation characteristics of microseismic waves, and discussed the attenuation responses of seismic wave energy to the seismic source energy, radius, energy attenuation coefficient, and the distance from the seismic source to the loaded point during large-scale rupture. Liu et al.[21] extracted the microseismic waveforms and spectral characteristics under different energy levels based on field microseismic data. Jing et al.[22] performed wavelet noise reduction on the original microseismic signal to obtain the distribution characteristics of signal energy, and analyzed the attenuation characteristics of the instantaneous energy during the propagation of microseismic signals by using the Hilbert-Huang transform (HHT). Zhang et al.[23] employed the VMD method to obtain the energy distribution characteristics and identify the rock fracture and blast vibration signals. Zhou et al.[24] used VMD to process the microseismic signals of the mine and obtained the energy-frequency relationship of each mode of microseismic signals. Jia et al.[25] established the wavefront equation for microseismic wave under non-uniform medium conditions and revealed the influence of specific geological conditions such as faults and goaf on the propagation of microseismic signals.

Based on the previous research, the changes in propagation characteristics of microseismic signals in specific geological structures need to be further studied. The objective of this study is to investigate the attenuation characteristics of microseismic signal energy in the "three-zone" structure of the goaf, and to clarify the relationship between the microseismic signal energy and the signal frequency. In this paper, we conduct a model test on the overburden structure in the goaf, decompose the signals into intrinsic mode functions (IMFs) with limited bandwidth by using VMD, calculate the energy of the signals in different frequency bands, and then fit the signal energy to the central frequency. This will elucidate the changes of the signal energy in the frequency domain, and provide a reference for the attenuation of microseismic signals in the "three-zone" structure of the goaf.

## 2 Principles of VMD and microseismic signal energy calculation

### 2.1 VMD principle

VMD is a non-recursive signal decomposition method for adaptive solving. It transforms the mode estimation into a variational problem, and then iteratively searches for the optimal solution of the constrained variational model[6]. This method is employed to decompose the real-valued input signal $f$ into a finite number of sub-signals $u_k$. Each mode has its own central frequency $\omega_k$.

The mode function is defined as an amplitude-modulation and frequency-modulation (AM-FM) signal, denoted as follows[6]:

$$u_k(t) = A_k(t)\cos(\varphi_k(t)) \quad (1)$$

where $t$ is the time; $u_k(t)$ is the sub-signal according to VMD; $A_k(t)$ is the instantaneous amplitude of the sub-signal, and $A_k(t) \geqslant 0$; $\varphi_k(t)$ is the instantaneous phase of the sub-signal, which is a non-decreasing function, and $\varphi_k(t) \geqslant 0$. $\omega_k(t) = \varphi_k(t)$ is the central frequency of the sub-signal.

The Hilbert transform is made for the mode function $u_k$ and the resulting spectrum is shifted to the baseband using the estimated central frequency. The bandwidth is then estimated by calculating the square of the L2 norm of its gradient, resulting in following constrained variational model[6]:

$$\min_{\{u_k\},\{\omega_k\}} \left\{ \sum_k \left\| \partial_t \left[ (\delta(t) + \frac{j}{\pi t}) * u_k(t) \right] \mathrm{e}^{-j\omega_k t} \right\|_2^2 \right\} \quad (2)$$
$$\text{s. t.} \quad \sum_k u_k(t) = f(t)$$

where $\{u_k\}=\{u_1, ..., u_k\}$ is the set of all modes; $\{\omega_k\}=\{\omega_1, ..., \omega_k\}$ is the central frequency corresponding to each mode; $\delta(t)$ is the Dirac function; * is the convolution symbol; and $f(t)$ is the real-valued input signal. The constraint is that the sum of each mode is equal to the input signal.

To guarantee the model convergence and strict enforcement of constraints, the penalty factor $\alpha$ and Lagrange multiplier $\lambda$ are used to transform the original constrained variational problem (Eqs. (1) and (2)) into an unconstrained variational problem. The augmented and generalized Lagrangian function $L$ is then expressed as follows[6]:

$$L(\{u_k\},\{\omega_k\},\lambda)=\alpha\sum_k\left\|\partial_t\left[(\delta(t)+\frac{j}{\pi t})*u_k(t)\right]\times \mathrm{e}^{-j\omega_k t}\right\|_2^2+\left\|f(t)-\sum_k u_k(t)\right\|_2^2+\left\langle\lambda(t),f(t)-\sum_k u_k(t)\right\rangle \quad (3)$$

where $\alpha$ is the quadratic penalty factor; and $\lambda(t)$ is the Lagrange multiplier.

By solving the optimal solution of the above variational model, i.e. the saddle point of the augmented Lagrangian function $L$, the mode function $u_k$ and central frequency $\omega_k$ can be expressed as follows[6]:

$$\hat{u}_k^{n+1}(\omega)=\frac{\hat{f}(\omega)-\sum_{i\neq k}\hat{u}_i(\omega)+\dfrac{\hat{\lambda}(\omega)}{2}}{1+2\alpha(\omega-\omega_k)^2} \quad (4)$$

$$\omega_k^{n+1}=\frac{\int_0^\infty\omega\left|\hat{u}_k(\omega)\right|^2\mathrm{d}\omega}{\int_0^\infty\left|\hat{u}_k(\omega)\right|^2\mathrm{d}\omega} \quad (5)$$

where $\hat{u}_k^{n+1}(\omega)$, $\hat{f}(\omega)$, $\hat{u}_i(\omega)$ and $\hat{\lambda}(\omega)$ are the Fourier transforms of $u_k^{n+1}(t)$, $f(t)$, $u_i(t)$ and $\lambda(t)$; and $n$ is the iteration step. By making the inverse Fourier transform of the desired $\hat{u}_k(\omega)$ and taking its real part, the time domain mode $u_k(t)$ can be obtained.

### 2.2 Principle of microseismic signal energy calculation

In the microseismic monitoring applications, the original microseismic data are often used to calculate the signal energy. By introducing a common concept in signal and system analysis, the signal energy is calculated as

$$E_{\mathrm{S}}=\lim_{T_{\mathrm{S}}\to\infty}\int_{-T_{\mathrm{S}}}^{T_{\mathrm{S}}}\left|f(t)\right|^2\mathrm{d}t \quad (6)$$

where $E_{\mathrm{S}}$ is the signal energy; $T_{\mathrm{S}}$ is the integration interval; and $f(t)$ is the signal function.

The integration time of the microseismic signal is infinite, making it suitable for a wide range of applications. However, the microseismic signal is time-varying and non-periodic. It can be regarded as a finite duration vibration signal after filtering out the background noise. Therefore, the microseismic signal energy is calculated by taking the finite time containing the vibration signal:

$$E_{\mathrm{ms}}=\int_{t_1}^{t_2}\left|f(t)\right|^2\mathrm{d}t \quad (7)$$

where $E_{\mathrm{ms}}$ is the microseismic signal energy; and $t_1$ and $t_2$ are the time limits.

In the process of microseismic signal acquisition, the occurrence time of the seismic activity is not controllable, resulting in a large difference in the duration of vibration signals collected by the sensors. In order to reduce this difference, the interception processing of the original signal is required. The peak vibration velocity $V_{\max}$ of the original signal is first picked up to determine the peak arrival moment. Then, the time limits $t_1$ and $t_2$ are determined by taking $\Delta t$ before and after the peak arrival moment, respectively, to ensure that the intercepted signal completely contains the signal duration. Finally, the signal in the time interval $[t_1, t_2]$ is used as the microseismic signal $V_0(t)$ to be analyzed.

The microseismic data acquisition is performed at a fixed sampling frequency $f_{\mathrm{s}}$ with a sampling interval of $\Delta t = 1/f_{\mathrm{s}}$. The number of vibration signal samples is $N=(t_2-t_1)/\Delta t =(t_2-t_1)f_{\mathrm{s}}$, and the sampled signal is a discrete time series, which is expressed in Eq. (8) as a discrete form of Eq. (7) to calculate the $V(m)$ signal energy.

$$E_{\mathrm{ms}}=\sum_{m=1}^{N}V^2(m)\Delta t \quad (8)$$

where $m$ is the serial number of the samples; and $N$ is the number of samples.

## 3 Modeling of overburden structure in the goaf

### 3.1 Model test

According to the relevant geological and mining data of a mine including the histogram of a fully mechanized mining face and the physico-mechanical properties of rocks, as well as the dimensions of the frame system (2.8 m×0.3 m×1.5 m, plane-stress model test platform), the similarity ratios of geometry, gravity, strength and time are determined to be 1:200, 1:1.7, 1:340 and 1:14 based on the principle of similarity conditions. After analysis, the test model can accurately reflect the stratigraphic state in the field and fulfill the conditions of this study. The model uses sand as aggregate, and lime and gypsum as cementing materials, which are mixed in different proportions to simulate various rock formations[15]. The distribution of each rock layer in the model and its physical properties are listed in Table 1. The schematic diagram of the layered media is plotted in Fig. 1 based on the parameters of a similar model, where ASA, ASB and ASC represent the seismic sources.

The open-off cut with a length of 50 mm is excavated 500 mm from one side of the model. Thereafter, the mining operation is carried out. After mining, the overburden structure above the goaf exhibits the formation of "three zones", i.e. caving zone, fissure zone and sagging zone, as shown in Fig. 1[15].

**Table 1 Distribution of rock layers and their physical parameters[26]**

| Rock formation | No. of rock formation | Thickness of rock formation/mm | Proportion of mixture | Strength of rock formation/kPa | |
|---|---|---|---|---|---|
| | | | | Compressive | Tensile |
| Mudstone | s25 | 36(66) | 573 | 65 | 5 |
| Sandy mudstone | s24 | 28 | 573 | 63 | 4 |
| Medium-grained sandstone | s23 | 54 | 455 | 201 | 10 |
| Mudstone | s22 | 25 | 573 | 65 | 4 |
| E11 coal | s21 | 12 | 637 | 25 | 5 |
| Sandy mudstone | s20 | 44 | 573 | 63 | 4 |
| Fine sandstone | s19 | 27 | 355 | 248 | 13 |
| Mudstone | s18 | 115 | 573 | 65 | 5 |
| Medium-grained sandstone | s17 | 29 | 455 | 201 | 10 |
| Mudstone | s16 | 224 | 573 | 65 | 5 |
| Medium-grained sandstone | s15 | 56 | 455 | 201 | 10 |
| Fine sandstone | s14 | 48 | 355 | 248 | 13 |
| Mudstone | s13 | 30 | 573 | 65 | 5 |
| Siltstone | s12 | 90 | 537 | 171 | 6 |
| Medium-grained sandstone | s11 | 55 | 455 | 201 | 10 |
| Sandy mudstone | s10 | 53 | 573 | 63 | 4 |
| Fine sandstone | s9 | 42 | 355 | 248 | 13 |
| Mudstone | s8 | 28 | 573 | 65 | 5 |
| Fine sandstone | s7 | 12 | 355 | 248 | 13 |
| Mudstone | s6 | 27 | 573 | 65 | 5 |
| F16−17 coal | s5 | 30 | 637 | 25 | 5 |
| Sandy mudstone | s4 | 51 | 573 | 63 | 4 |
| Mudstone | s3 | 12 | 573 | 65 | 5 |
| Limestone | s2 | 53 | 573 | 63 | 4 |
| Mudstone | s1 | 19(31) | 573 | 65 | 5 |

Note: Regarding the thicknesses of rock formations s1 and s25, the numbers in the parentheses are the actual layer thicknesses of the model, and the numbers outside the parentheses are the thicknesses of the media contained in the study area. The first digit of the proportion of mixture is the sand-to-cement ratio, and the second and third digits represent the lime and gypsum percentages of the cementing material, respectively.

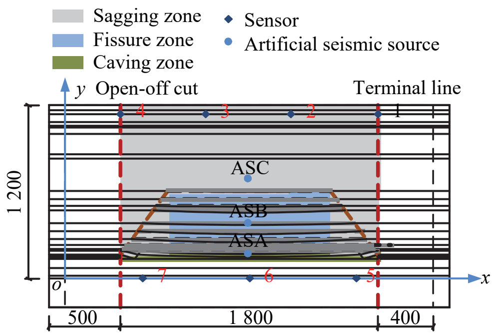


**Fig.1 Schematic diagram of mined-out subsidence area in layered media (unit: mm)**

The blast impact signal is characterized by short rise time and short duration of peak signal. The waveform characteristics of the impact signal generated by the pendulum after a single impact are similar to that of the blast impact signal. Hence, the pendulum is used as an artificial vibration-generating device to simulate the blast impact signal. After the formation of the goaf, a pendulum with a length of 70 cm and a mass of 30 g was employed as the seismic source excitation device. The location of the seismic source is shown in Fig. 1, and the location coordinates of the seismic sources are listed in Table 2. An infrared timer is used to record the seismic source moment, and it synchronously starts with the microseismic monitoring device. When the pendulum hits the predetermined seismic source, the pendulum line cuts the infrared ray to register the occurrence time $t_0$ of the seismic activity[15].

**Table 2 Artificial seismic source position coordinates and occurrence time**

| Seismic source | $x$/mm | $y$/mm | Occurrence time $t_0$/s |
|---|---|---|---|
| ASA | 1 297.32 | 174.00 | 6.411 722 |
| ASB | 1 300.87 | 385.14 | 8.006 455 |
| ASC | 1 300.98 | 692.59 | 2.868 796 |

After exciting the artificial seismic source, the microseismic signals are collected by Antenna-III. The observation range of the equipment is from −3 to 2, and the maximum sampling frequency can be up to 100 kHz. In this test, the sampling frequency is set to 100 kHz. The sensor is of non-directional type, and it collects signals in the direction of the maximum vibration velocity[15]. Figure 1 shows the locations of the sensors, and Table 3 lists their coordinates. The signals recorded by the sensors are displayed in Fig. 2.

**Table 3 Sensor position coordinates**

| Sensor No. | $x$/mm | $y$/mm |
|---|---|---|
| 1 | 2 200 | 1 140 |
| 2 | 1 600 | 1 140 |
| 3 | 1 000 | 1 140 |
| 4 | 400 | 1 140 |
| 5 | 550 | 0 |
| 6 | 1 300 | 0 |
| 7 | 2 050 | 0 |

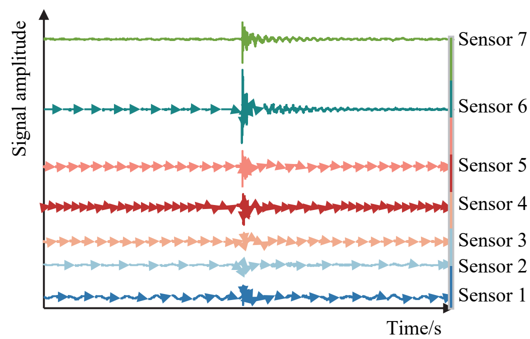


**Fig.2 Artificial seismic source excitation of original microseismic signal (in ASA)**

### 3.2 Intercepted signals and signal energy

In the simulation test, an artificial seismic source is used to generate the signals. The duration of the signal acquired by the sensor varies greatly, thus it is necessary to perform signal interception processing on the original signal. The sampling frequency is 100 kHz. To ensure the integrity of the intercepted signal, the target signal before and after the peak signal within the time limit $\Delta t = \pm 0.5$ s is selected. The target signal energy is calculated by Eq. (8). The energies of the target signals are tabulated in Table 4.

**Table 4 Target signal energies**

| Seismic source | Target signal energy/($mm^2 \cdot s^{-1}$) | | | | | | |
|---|---|---|---|---|---|---|---|
| | 1 | 2 | 3 | 4 | 5 | 6 | 7 |
| ASA | $1.243\times10^{-4}$ | $5.290\times10^{-5}$ | $6.308\times10^{-5}$ | $1.177\times10^{-4}$ | $1.018\times10^{-4}$ | $3.450\times10^{-4}$ | $1.082\times10^{-4}$ |
| ASB | $7.937\times10^{-5}$ | $7.444\times10^{-5}$ | $7.437\times10^{-5}$ | $2.094\times10^{-4}$ | $5.262\times10^{-5}$ | $8.938\times10^{-5}$ | $6.679\times10^{-5}$ |
| ASC | $8.204\times10^{-5}$ | $1.207\times10^{-4}$ | $1.388\times10^{-4}$ | $1.697\times10^{-4}$ | $2.547\times10^{-5}$ | $5.651\times10^{-5}$ | $3.430\times10^{-5}$ |

## 4 VMD-based calculation of microseismic signal energy

### 4.1 Optimal number of mode components for VMD of microseismic signals

The central frequency observation method is employed to determine the optimal number of mode components. According to the results of trial calculation, the number of mode components $K$ for the VMD process of target signal takes 2−12 in sequence, and the empirical values are assigned to other parameters. The central frequencies of each mode component when the number of mode components $K$ of the signal received by the sensor No. 1 under the seismic source ASA ranges from 2 to 10 are listed in Table 5. When $K$ is equal to 2, the central frequencies of mode components are 261.52 Hz and 30.37 Hz, showing a large difference in the central frequencies of different mode components. When $K$ is equal to 8, the central frequencies of mode components are 383.25 Hz and 229.66 Hz, which are close to each other. When $K$ is equal to 10, the central frequencies of mode components are 422.26 Hz and 413.36 Hz, with almost identical central frequencies. When $K$ is further increased to 11 and 12, the central frequencies of mode components are 413 Hz, 408.18 Hz and 467.78 Hz, 397.42 Hz, respectively, which are very similar, indicating an over-decomposed state of the signal at this time. As the optimal number of decomposed layers is assumed to be equal to the previous $K$ value when the central frequencies are close to each other, the optimal number of mode components is determined to be 7. The distribution of the optimal number of mode components of other seismic source signals is shown in Fig. 3. One can see that the maximum value of the optimal number of mode components for each sensor under the seismic source ASA is 8, while the minimum value is 7. The maximum value of the optimal number of mode components for each sensor under the seismic source ASB is 11, while the minimum value is 6. The maximum value of the optimal number of mode components for each sensor under the seismic source ASC is 10, while the minimum value is 6. Therefore, in the modeling test of the overburden structure in the goaf, the effective number of mode components for the artificial pendulum-excited vibration signal ranges from 6 to 11, which are all within

**Table 5 Central frequencies of each mode component for different *K* values of ASA-1**

| $K$ | Central frequency/Hz | | | | | | | | | | | |
|---|---|---|---|---|---|---|---|---|---|---|---|---|
| 2 | 261.52 | 30.37 | — | — | — | — | — | — | — | — | — | — |
| 3 | 597.57 | 235.07 | 25.14 | — | — | — | — | — | — | — | — | — |
| 4 | 613.02 | 246.43 | 140.94 | 22.00 | — | — | — | — | — | — | — | — |
| 5 | 912.17 | 508.09 | 237.54 | 97.08 | 21.12 | — | — | — | — | — | — | — |
| 6 | 1 392.72 | 836.20 | 493.74 | 236.41 | 94.74 | 21.16 | — | — | — | — | — | — |
| 7 | 1 476.72 | 997.85 | 761.58 | 473.93 | 234.46 | 94.08 | 21.10 | — | — | — | — | — |
| 8 | 18 061.12 | 1 411.42 | 861.53 | 565.83 | 383.25 | 229.66 | 87.63 | 21.02 | — | — | — | — |
| 9 | 31 447.29 | 13 364.10 | 1 413.25 | 864.17 | 567.23 | 378.96 | 229.55 | 87.11 | 21.04 | — | — | — |
| 10 | 31 553.10 | 13 819.43 | 5 408.93 | 1 393.52 | 834.91 | 422.26 | 413.36 | 227.05 | 84.58 | 21.00 | — | — |
| 11 | 31 509.58 | 18 573.79 | 7 726.55 | 1 609.21 | 1 145.34 | 810.49 | 413.00 | 408.18 | 226.74 | 84.20 | 20.97 | — |
| 12 | 31 500.71 | 18 341.81 | 7 726.49 | 1 657.80 | 1 287.86 | 906.33 | 708.36 | 467.78 | 397.42 | 226.59 | 83.43 | 21.00 |

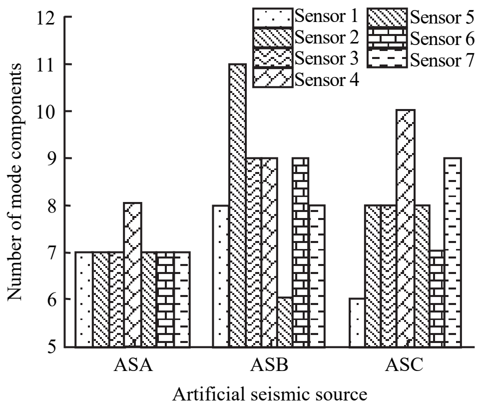


**Fig.3 Numbers of optimum modes for seismic source signals**

the range of the selected values for the number of mode components in the VMD process.

### 4.2 Calculation of microseismic signal energy

According to the determined optimal number of mode components, the IMFs of the microseismic signal at different central frequencies are obtained. Figure 4 shows the set of each IMF and the corresponding spectrum of the signal received by the sensor No. 2 under the seismic source ASA. From this figure, it is evident that IMF1 is a high-frequency noise component with a central frequency of 22 784.16 Hz, which is analogous to a high-frequency carrier wave, and the mode waveform has no source generation features. IMF7 is a low-frequency noise component with a central frequency of 15.86 Hz, which is similar to a low-frequency carrier wave. The seismic wave features can be seen, but the peak mode amplitude is nearly $6\times10^{-3}$ mm/s, which is 10 times smaller than that of the original signal. Therefore, it is considered as a non-primary seismic mode and thus should be excluded. According to the spectral division of vibration events by Cai et al.[27], the frequency of microseismic events ranges from 100 Hz to 1 000 Hz. In conjunction with the waveforms and spectral characteristics of the mode components shown in Fig. 4, the modes with central frequency in the range of 16-5 000 Hz are taken as the effective modes, and then the reconstructed microseismic signals $V(t)$ are obtained, as plotted in Fig. 5. From this figure, it is obvious that the waveform becomes straight before the arrival of the signal, and the peak vibration velocity is almost unaffected by the filtering process. For any other microseismic signal, the range of effective frequency band is determined according to the central frequency value of the noise component in the optimal decomposition state.

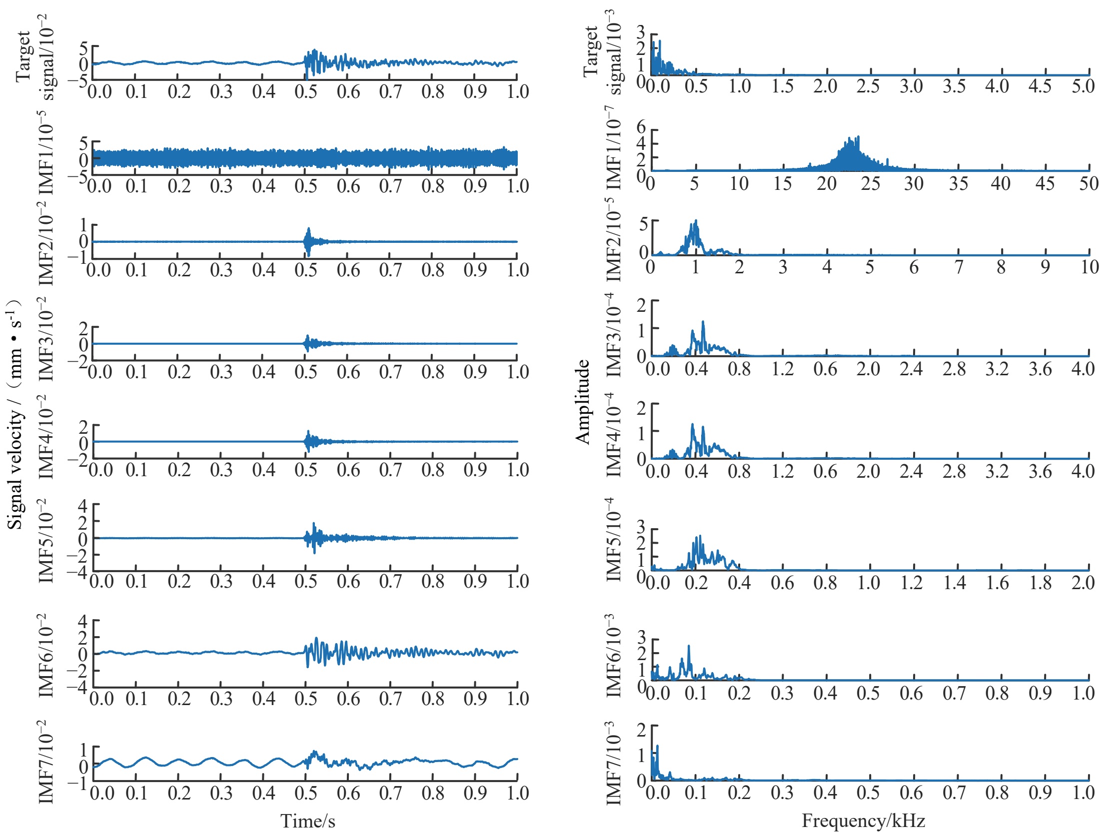


(a) VMD (b) Frequency

**Fig.4 Modal components and frequency spectra for ASA-2 signal**

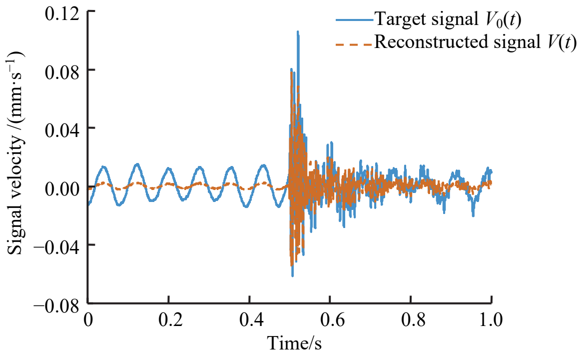


**Fig.5 Comparisons of ASA-2 microseismic signals before and after reconstruction**

The reconstructed microseismic signal $V(t)$ for each sensor under each seismic source is obtained following the above filtering procedure. The signal energy of each mode is calculated according to Eq. (8). Figure 6 shows that the signal energy in the initial state of the VMD process is stable. With the increase in number of mode components, the signal energy decreases slightly. As $K$ continues to increase, there is a sudden drop of signal energy. With the increase in $K$, the signal energy is still decreasing slightly. When the number of mode components approaches the maximum value, the signal energy gradually increases and is eventually maintained stable. The sensor No. 7 under the seismic source ASA is taken as an example. The signal is in an incomplete decomposition state at the initial stage of decomposition, and the central frequencies of mode components are approximately 313 Hz and 43 Hz when the number of mode components is 2. When the number of mode components is 5, the central frequencies of mode components are approximately 1 595, 755, 327, 200 and 28 Hz, and the effective components of the signal are not completely decomposed. Before reaching the optimal number of mode components, there is mode aliasing phenomenon occurred in each component. The low-frequency invalid signal remains undecomposed and unfiltered, which results in part of low-frequency noise being included in energy calculation. Therefore, there is almost no obvious change in signal energy after filtering compared to the target signal energy. This same performance is also observed with the seismic sources ASB and ASC.

When the number of mode components is 7, the effective components of the signal are completely decomposed and filtered, most of the low-frequency noise signals can be effectively removed, and the signal energy is greatly reduced. As the decomposition proceeds, the low-frequency signal contains a small amount of unfiltered low-frequency signal, which is gradually decomposed and filtered, and the signal energy is still slowly reduced. Compared with the target signal energy, in the state of complete decomposition, after filtering and removing the signal noise, the signal energy is reduced from $1.082 \times 10^{-4}$ mm$^2$·s$^{-1}$ to $6.028 \times 10^{-5}$ mm$^2$·s$^{-1}$, by nearly 50% of the total signal energy. The seismic sources ASB and ASC also have the similar performance.

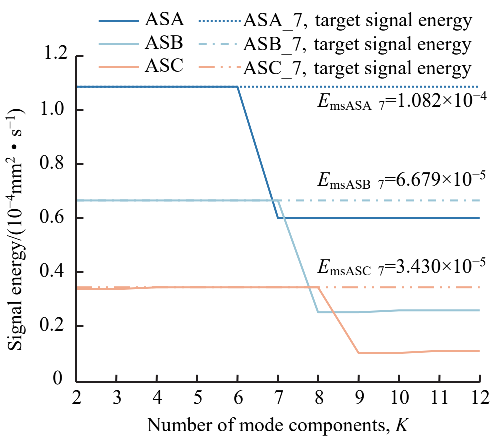


**Fig.6 Signal energies at different *K* values for ASB_7, ASA_7 and ASC_7**

When the number of mode components increases to 12, the central frequencies are 39 323, 31 494, 22 984, 12 696, 2 948, 2 087, 1 866, 1 598, 1 324, 880, 657, 433, 316, 190 and 26 Hz. At this time, the signal is over-decomposed, the high-frequency noise component due to the over-decomposition is filtered, and the signal energy magnitude is basically maintained as that in the complete decomposition state. However, due to the over-decomposition of the IMFs in the intermediate frequency band and the unfiltered spurious components obtained, the signal energy is slightly increased compared to that in the full decomposition state. The seismic sources ASB and ASC also exhibit similar performance.

One can see from Table 6 that the number of mode components of the signal received by the sensor No. 7 under the seismic source ASA is assumed to be 10. After decomposition, the central frequencies and energies of each mode component greater than 5 000 Hz are 31 819.77, 19 835.06 Hz and $4.14\times10^{-11}$, $4.54\times10^{-11}$ mm$^2$·s$^{-1}$, while the central frequency and energy of mode component less than 50 Hz are 21 Hz and $4.90\times10^{-5}$ mm$^2$·s$^{-1}$. The energy of the high-frequency signal component (the central frequency is greater than 5 000 Hz) accounts for only 0.000 3% of the total signal energy, while the energy of the low-frequency signal component (the central frequency is less than 50 Hz) accounts for 47.426 5%, indicating that the low-frequency signal component contains most of the signal energy. Therefore, decomposing and filtering the low-frequency noise is the key to calculating and analyzing the signal energy, and it is of great significance to understand the characteristics of signal energy.

**Table 6 Energy share of each mode for ASA-7 signal**

| Mode component | Central frequency /Hz | $E_{ms}$/(mm$^2$ • s$^{-1}$) | Energy share/% |
|---|---|---|---|
| IMF1 | 31 819.77 | $4.14\times10^{-11}$ | 0.000 1 |
| IMF2 | 19 835.06 | $4.54\times10^{-11}$ | 0.000 1 |
| IMF3 | 1893.39 | $3.18\times10^{-8}$ | 0.038 5 |
| IMF4 | 1464.05 | $5.47\times10^{-8}$ | 0.066 2 |
| IMF5 | 965.40 | $2.13\times10^{-7}$ | 0.257 6 |
| IMF6 | 763.06 | $6.98\times10^{-7}$ | 0.844 9 |
| IMF7 | 453.60 | $2.32\times10^{-6}$ | 2.812 7 |
| IMF8 | 316.54 | $2.45\times10^{-5}$ | 29.597 9 |
| IMF9 | 191.80 | $1.57\times10^{-5}$ | 18.955 6 |
| IMF10 | 26.86 | $3.92\times10^{-5}$ | 47.426 5 |

### 4.3 Relationship between microseismic signal energy and frequency

To explore the relationship between energy and frequency of microseismic signals, the relationship between the full mode frequency of the signal and the mode energy is established by using a scatter plot with frequency on the horizontal axis and mode energy on the vertical axis. Based on the distribution of the data points, a Gaussian function model can be used to fit the relationship, which is expressed as follows:

$$y = a\mathrm{e}^{-\frac{(x-b)^2}{c^2}} \qquad (9)$$

where $a$ is the peak value of the fitting curve; $b$ is the peak coordinate of the fitting curve; and $c$ is the width of the "bell" of the fitting curve.

The curve fitting is performed by using the robust regression with fitting accuracy of $10^{-6}$. The maximum numbers of function calculations and iterations allowed are taken as 1 000. The Gaussian fitting results are shown in Fig. 5. The coefficient of determination $R_{\text{adj}}^2$ (adjusted $R^2$) and RMSE are the evaluation indices of the fitting results, and both are within the range [0, 1]. When $R_{\text{adj}}^2$ is close to 1, and RMSE tends to 0, the independent variable can better reflect the response variable through the fitting process, and the fitting effect is better. The correlation coefficient $R$ between 0.7 and 1.0 indicates a strong correlation, 0.5−0.7 shows medium correlation, 0.3−0.5 indicates weak correlation, and 0−0.3 shows no correlation. For this paper, $R^2$ from 0 to 0.09 corresponds to no correlation, and 0.09−1 shows correlation.

$$R_{\text{adj}}^2 = 1 - \left(\frac{N-1}{N-P}\right)\frac{\sum_{i=1}^{N} w_i (y_i - \hat{y}_i)^2}{\sum_{i=1}^{N} w_i (y_i - \bar{y}_i)^2} \qquad (10)$$

$$\text{RMSE} = \sqrt{\frac{1}{N}\sum_{i=1}^{N} w_i (y_i - \hat{y}_i)^2} \qquad (11)$$

where $w_i$ is the sample weight of the data; $y_i$ is the original data; $\hat{y}_i$ is the predicted data; $\bar{y}_i$ is the mean of the original data; $N$ is the number of samples; and $P$ is the number of regression coefficients.

Figure 7 indicates that the coefficients of determination for the three seismic sources are all larger than 0.9. This suggests that the numerical relationship between mode energy and frequency can be approximated by a Gaussian function. The mode energy shows a tendency to increase and then decrease with the increase in frequency. This is consistent with the basic characteristics of a Gaussian distribution, and the signal energy is mainly concentrated in the frequency range of 10−2 000 Hz. However, due to the different locations of the seismic sources and the various rock layers encountered during the signal propagation process, the differences in peak center and the width of the bell shape of the Gaussian distribution are induced. Meanwhile, the central frequency of the energy peak changes from 36.19 Hz under the seismic source ASB to 1 153 Hz under the seismic source ASA, representing a 95% increase in central frequency. The central frequency of the energy peak under the seismic source ASC is 1 182 Hz, with a 95% increase in central frequency compared with the seismic source ASA. It can be concluded that different rock layers, goafs and faults in the complex geological model have different degrees of frequency modulation on the seismic source, which indicate differences in Gaussian fitting for different propagation states. Meanwhile, we can characterize the difference of energy-frequency distribution of the signal by determining the fitting function to locate the seismic source in the "three-zone" structure of the goaf.

In the optimal decomposition state of the signal, the mode energy and the corresponding central frequency are used for drawing a scatter plot, which can determine the relationship between energy and central frequency of each mode component by fitting. A power function model is proposed for the seismic sources ASA, ASB and ASC, based on the scatter plot of each mode energy and frequency of the signal received by the sensor No. 1, and it is expressed as follows:

$$y = ax^b \qquad (12)$$

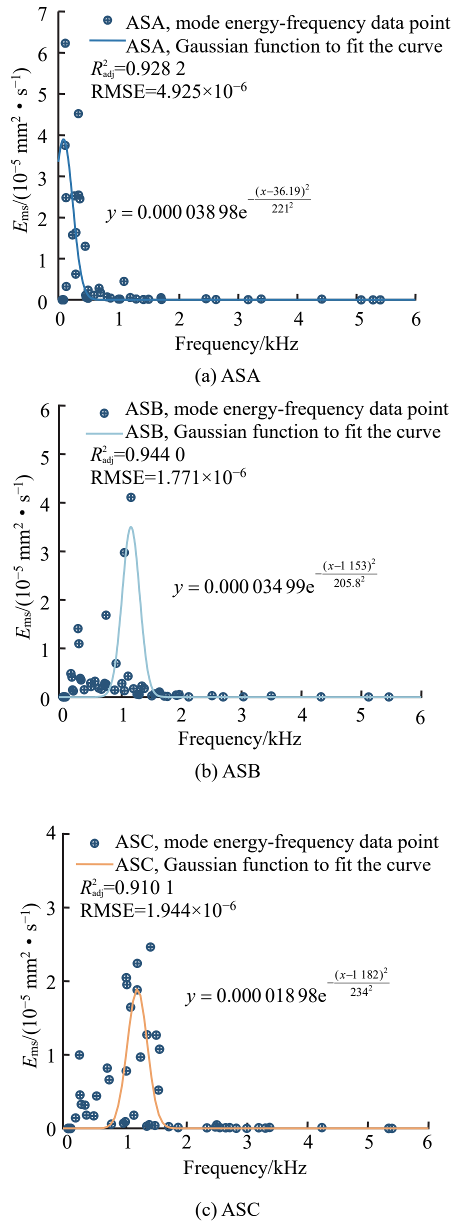


**Fig.7 Relationships between energy and central frequency for three signals**

During the fitting process, the fitting accuracy is $10^{-6}$, and the maximum number of function calculations and iterations allowed are set to 1 000. The fitting results are shown in Fig. 8. According to the fitting results listed in Table 7, the coefficients of determination for the signals recorded by the sensor No. 1 under three seismic sources are all greater than 0.9. It can be considered that the energy of each mode component is power-exponentially correlated with the central frequency. The signal energy decreases as the frequency increases, and it is mainly concentrated in the frequency band from 0 to 2 000 Hz. According to the positional relationship of each fitting function, it can be observed that the attenuation rate of the signal energy under the seismic source ASA located in the caving zone is faster than that of the seismic sources ASB and ASC. Therefore, it can be assumed that due to the differences in the structural location and propagation state of the seismic source, the signal energy attenuation trend of each sensor is different, and the signal attenuation speed is faster in the caving zone.

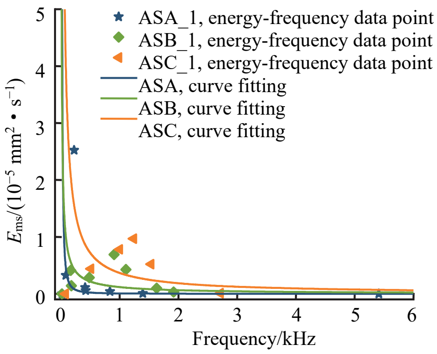


**Fig.8 Relationships between signal modal energy and central frequency (sensor No. 1)**

**Table 7 Fitting results of signal modal energy and central frequency for different seismic sources at sensor No. 1**

| Sensor | Fitting parameter | | $R^2_{adj}$ | RMSE |
|---|---|---|---|---|
| | *a* | *b* | | |
| ASA-1 | 0.009 039 0 | −1.715 0 | 0.998 6 | $6.313\times10^{-7}$ |
| ASB-1 | 0.000 504 7 | −0.878 1 | 0.944 5 | $3.166\times10^{-6}$ |
| ASC-1 | 0.003 041 0 | −0.973 1 | 0.918 2 | $4.440\times10^{-6}$ |

## 5 Analysis of signal energy response to "three-zone" structure

### 5.1 Signal energy change in "three-zone" structure

In the test model, the seismic sources ASA, ASB and ASC are located in the caving zone, fissure zone and sagging zone, respectively. In the "three-zone" structure, the compaction of the sagging zone is good. However, due to irregular rock mass caused by strata collapse, rock bodies in the caving zone are not well compacted. The fissure zone contains a large number of fissures, and has a poorer compaction than the sagging zone, but better than that of the caving zone. The signals from the seismic source ASA arrive at sensors Nos. 1−4 through the caving zone, fissure zone and sagging zone. The signals from the seismic source ASC travel downwards through the sagging zone, fissure zone and caving zone to sensors Nos. 5−7. The energies recorded by the sensors under the seismic sources ASA and ASC are shown in Fig. 9.

Comparing the energies registered by the sensors Nos. 2, 3 and 4, the energies under the seismic source ASC is larger than that under the seismic source ASA. The signals from the seismic source ASA arrive at the sensors Nos. 1−4 through caving zone, fissure zone and sagging zone in the upward direction, which are farther from the sensors than those of ASC. The signal energies registered by the sensors under the seismic source ASA are reduced by 40.63%, 24.64% and 74.06% compared with those of ASC, which is a significant reduction in attenuation amplitude. Comparing the energies recorded by the sensors No. 5, 6 and 7, the energies under the seismic source ASA are larger than those under ASC. The microseismic waves from the seismic source ASC travel downwards to the sensors Nos. 5−7 through the sagging zone, fissure zone and caving zone. The energies of the signals from the seismic source ASC recorded by the sensors are reduced by 92.37%, 96.80% and 83.15% compared with those of ASA, with an obvious attenuation.

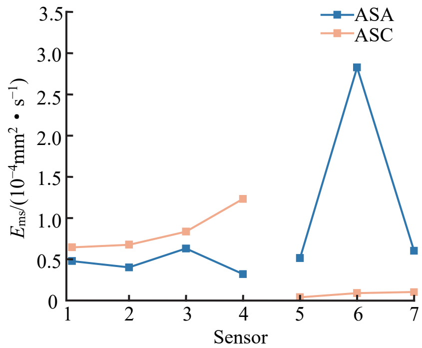


**Fig.9 Signal energies of each sensor for different seismic sources**

The microseismic waves from the seismic source ASB travel upwards through the fissure zone and sagging zone to the sensors Nos. 2, 3 and 4, and downwards through fissure zone and caving zone to the sensors Nos. 5, 6 and 7. The distance of the seismic source ASB from sensor No. 3 is 1 213 mm, which is much larger than that of the sensor No. 7 (488.2 mm). However, the energy registered by the sensor No. 3 ($1.479\ 8\times10^{-4}$ mm$^2$/s) is much larger than that recorded by the sensor No. 7 ($3.319\ 3\times10^{-5}$ mm$^2$/s), showing that the far-point energy exceeds the near-point energy. For the sensor No. 6, the downward signal energy attenuation under ASB compared to ASA is 88.26%, while that under ASC compared to ASA is 96.80%, showing a significant attenuation in both cases.

The above analysis indicates that the energy attenuation during the upward propagation process ranges from 25% to 75%, while the energy attenuation during the downward propagation process ranges from 85% to 95%. The differences in the number of structural layers and the sequence of crossing these layers result in varying degrees of attenuation effects on the energy when the microseismic waves traverse the goaf. Through comparative analysis of the sensor energy under the seismic source ASB, it is evident that the energy is attenuated relative to the distance between the sensor and the seismic source, and there are differences in the influence of the relative distance on the degree of energy attenuation. In the "three-zone" structure of the goaf, the rock layer of caving zone is completely fractured, and the rock body is irregular and poorly compacted, compared with the sagging zone and fissure zone. Therefore, the comparison of the energy recorded by the sensor No. 6 shows that the energy attenuation for the signals that travel through the caving zone is as high as 80%, which is much larger than that for the signals traveling through the sagging zone and fissure zone.

### 5.2 Signal energy-frequency relationship under "three-zone" structure

The microseismic signals arrive at the sensors through different layers. In order to investigate the relationship between energy and frequency in the signal propagation process within the "three-zone" structure, the signals of mode component at different central frequencies of each seismic source are obtained by using VMD, and the signals of effective component and their energies are calculated. The upward (towards sensors Nos. 1−4) and downward (towards sensors Nos. 5−7) propagation of the signals from the seismic source in different zones (the sagging zone, fissure zone and caving zone) are distinguished. The Gaussian function is still used to fit the relationship between the mode central frequency and mode energy. The statistics of the fitting results are listed in Table 8, where *a* is the peak value of the fitting curve, which indicates the signal energy; *b* is the horizontal coordinate of the peak of the fitting curve, which indicates the signal central frequency. The distribution of microseismic energy versus frequency is shown in Fig. 10.

**Table 8 Gaussian fitting results for energy versus frequency of microseismic signals in goaf**

| Seismic source | Fitting parameters | | | $R^2_{adj}$ | RMSE | Propagation direction and encountered layers |
|---|---|---|---|---|---|---|
| | *a* | *b* | *c* | | | |
| ASA | $1.535\times10^{-5}$ | 65.73 | 322.8 | 0.338 1 | $8.078\times10^{-6}$ | Upward, caving zone, fissure zone and sagging zone |
| | $1.181\times10^{-4}$ | 295.30 | 173.7 | 0.911 9 | $1.129\times10^{-5}$ | Downward, caving zone |
| ASB | $3.145\times10^{-5}$ | 1153.00 | 211.1 | 0.923 1 | $2.433\times10^{-6}$ | Upward, fissure zone and sagging zone |
| | $9.909\times10^{-6}$ | 271.80 | 193.8 | 0.543 9 | $3.160\times10^{-6}$ | Downward, fissure zone and caving zone |
| ASC | $1.879\times10^{-5}$ | 1401.00 | 270.2 | 0.874 3 | $2.649\times10^{-6}$ | Upward, fissure zone |
| | $1.956\times10^{-6}$ | 234.40 | 50.8 | 0.817 1 | $5.030\times10^{-7}$ | Downward, sagging zone, fissure zone and caving zone |

Figure 10 shows that the distribution of mode energy basically conforms to the Gaussian function, and the distribution characteristics of the energy in the frequency domain can be characterized by fitting the curve to the data. According to the fitting curves in Fig. 10(a), the peak for the upward signal from the seismic source ASA corresponds to the central frequency of 65.73 Hz, the peak for the seismic source ASB corresponds to the central frequency of 1 153 Hz, and the peak for the seismic source ASC corresponds to the central frequency of 1 401 Hz. The positions of the peaks on the fitting curves appear to be shifted to the right. The frequency change of ASB compared to ASA is 94.3%, and the frequency change of ASC compared to ASB is 17.7%, indicating an obvious frequency change. According to the fitting curves in Fig. 10(b), the signal energy corresponding to the peak for the downward signal from the seismic source ASA is $1.181\times10^{-4}$ mm$^2$/s, corresponding to the frequency of 295.3 Hz. The signal energy corresponding to the peak of the seismic source ASB is $9.90\times10^{-6}$ mm$^2$/s, corresponding to the frequency of 271.8 Hz. The signal energy corresponding to the peak of the seismic source ASC is $1.956\times10^{-6}$ mm$^2$/s, corresponding to the frequency of 234.4 Hz. Compared with the seismic source ASA, the peak values of the curves for the seismic sources ASB and ASC are reduced by 91.61% and 98.34%, respectively, while no noticeable change occurs for the peak position.

According to the changes in the fitting curves of each seismic source, the curve peaks and peak frequency changes under different propagation states are plotted, as shown in Fig. 11. For the signal frequency, the signal peak frequency of the seismic source ASA located in the sagging zone changes from 65.73 Hz in the upward direction to 295.3 Hz in the downward direction, with no obvious change; however, the peak frequencies of the seismic sources ASB and ASC in both upward and downward directions change from 1 153 Hz and 1 401 Hz to 271.8 Hz and 234.4 Hz, respectively. It seems that the central frequency of peak is obviously reduced.

The aforementioned analysis indicates that the microseismic signal propagates in the "three-zone" structure of the goaf, and the signal frequency is subjected to the frequency modulation of the structure. When the microseismic wave propagates upwards from the seismic source, it crosses fissure zone and sagging zone without passing through caving zone, and the central frequency of the microseismic signal varies slightly. However, when it crosses the caving zone and arrives at the sensor, due to the poor compaction of rock layers in this zone, the contact between the rock blocks completes the signal propagation, which is different from other structural zones. This results in a frequency change by more than 90%, which is obvious for the frequency modulation of central frequency.

For the signal energy, the upward and downward propagation distance for the seismic source ASB does not change much, but the peak height of the fitting curve decreases from 3.145 $\times10^{-5}$ mm$^2$/s in the upward direction to 9.909 $\times10^{-5}$ mm$^2$/s in the downward direction, with a significant decrease of 68.49%. The seismic source ASA is located in the caving zone, and the downward signal arrives at the sensors located in the caving zone. The medium does not change significantly, the distance from the sensors is closer, and the signal energy is at a high level. Thus, the microseismic signal propagates in the overburden structure of the goaf, and the signal energy is affected by the "three-zone" structure. Specifically, there is more obvious attenuation effect on signal energy in the caving zone compared to that in the sagging zone and fissure zone.

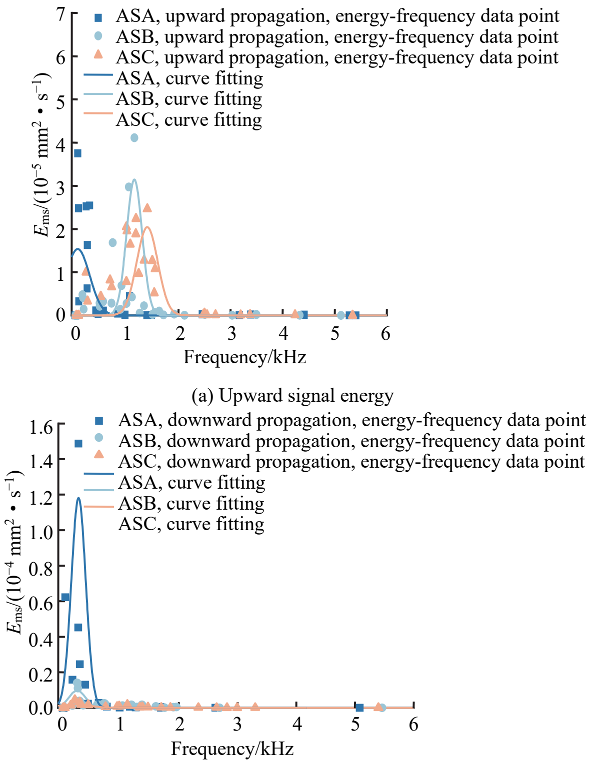


(b) Downward signal energy

**Fig.10 Relationships between microseismic energy and frequency distribution for overburden model of goaf**

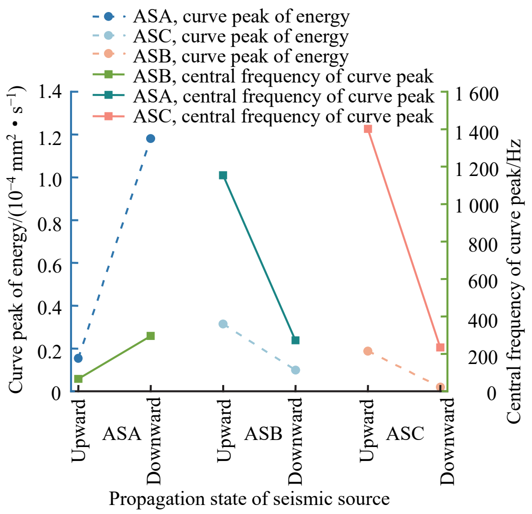


**Fig.11 Relationships between peak centers of seismic source energy distribution and seismic wave propagation state in a goaf**

## 6 Conclusions

Through VMD processing of microseismic signals in the model test in the overlying rock structure of the goaf, this study presents the relationship between signal energy and frequency, as well as the energy attenuation characteristics of the signals in the "three-zone" structure of the goaf. The following conclusions are reached:

(1) The processing of microseismic signals in the goaf based on VMD can effectively filter out the noise signals. When the microseismic signal is in the optimal decomposition state, it is filtered according to the central frequency of each mode component, and the effect of removing the high-frequency and low-frequency noise signals is obvious. In the VMD process of signals, the effective number of mode components of each microseismic signal in the simulation test ranges from 6 to 11, and there is a significant change in signal energy with the number of mode components $K$. This indicates that $K$ affects the results of signal energy calculation during signal decomposition by using VMD. Thus it is crucial to choose a reasonable and correct number of mode components for accurate signal energy calculation.

(2) The mode energy varies with the mode frequency following a power function. The signal recorded by the sensor No. 1 is fitted with a power function, and the coefficients of determination are greater than 0.9, indicating a good fit. With the increase in central frequency, the energy of mode component decreases following a power function. The signal energy of low-frequency component accounts for almost half of the total energy of the microseismic signals. The distribution of the energy of each mode component for the seismic signals in the frequency domain shows Gaussian single-peak characteristics, and the Gaussian function can be used to well fit the trend. During the signal propagation process, the changes in the peak center of the energy distribution occur as the microseismic wave crosses different structural surfaces, indicating that different geological structures have a frequency modulation effect on the microseismic waves. The peak values of these energy distributions also vary with the wave propagation across different structural surfaces, indicating that there are varying degrees of attenuation for wave energy in different geological layers.

(3) The microseismic waves exhibit varying attenuation effects as they traverse the "three-zone" structure of the goaf, due to the number and sequence of structural layers. In the model test, the upward signal shows an energy attenuation ranging from 25% to 75%, while the downward signal experiences an energy attenuation between 85% and 95%. The "three-zone" structure of the goaf exhibits the frequency modulation. The fitting results show a central frequency of 65.73 Hz for the seismic source in the caving zone, and the central frequencies of 1 153 Hz and 1 401 Hz for seismic source in the fissure zone and sagging zone, respectively. Notably, there is a significant variation in central frequency of up to 90%.

In the "three-zone" structure of the goaf, the rock layer in the caving zone is characterized by complete fracturing, irregularity, and poor compaction, compared with the fissure zone and sagging zone. Due to the variability in the nature of the rock layers, the effect of the caving zone on the energy attenuation is up to 80% and the effect of frequency modulation on the central frequency is up to 90%, which is much greater than that of the sagging zone and fissure zone. In the process of microseismic wave propagation, the energy attenuates with the relative distance between sensor and seismic source. In the model test, the far-point energy exceeds the near-point energy, indicating that the relative distance between seismic source and sensor has a different effect on the degree of energy attenuation.

The microseismic signals provide valuable information about the geological environment in the 'three-zone' structure of the goaf. The microseismic signal traverses the sagging zone, fissure zone and caving zone in the goaf, which exhibit distinct change characteristics. Consequently, variations in energy and frequency of the microseismic signal can accurately reflect the changes in geological structure. Removing the noise components from the signal is a crucial prerequisite for analyzing the changes in energy and frequency of the microseismic signals. Therefore, further research is needed to accurately and reasonably calculate the energy of the microseismic signals, and on this basis, to investigate the geological conditions of the complex strata in the goaf.

## References


[1] GUO Chao, CHEN Ying. Filtering technique for mining vibration signals and its affection on the signals' time-frequency characteristics[J]. **Journal of China Coal Society**, 2016, 41(7): 1859−1865.

[2] JIA Rui-sheng, ZHAO Tong-bin, SUN Hong-mei, et al. Microseismic signal denoising method based on empirical mode decomposition and independent component analysis[J]. **Chinese Journal of Geophysics**, 2015, 58(3): 1013−1023.

[3] MOUNIR NADA, OUADI HAMID, JRHILIFA ISMAEL. Short-term electric load forecasting using an emd-bi-lstm approach for smart grid energy management system[J]. **Energy & Buildings**, 2023, 288: 113022.

[4] LUO Ye-ke , CHEN Yong-gao, LI Sheng-cai. Adaptive denoising method of bridge vibration signal based on EWT-noise aided analysis theory[J]. **Journal of Vibration and Shock**, 2022, 41(21): 246−256.

[5] LIU H H, HAN M H. A fault diagnosis method based on local mean decomposition and multi-scale entropy for roller bearings[J]. **Mechanism and Machine Theory**, 2014, 75(5): 67−78.

[6] DRAGOMIRETSKIY KONSTANTIN, ZOSSO DOMINIQUE. Variational mode decomposition[J]. **IEEE Transactions on Signal Processing**, 2013, 62(3): 531−544.

[7] JIANG Xing-xing, SONG Qiu-yu, DU Gui-fu, et al. Review on research and application of variational mode decomposition[J]. **Chinese Journal of Scientific Instrument**, 2023, 44(1): 55−73.

[8] LIU Chang-liang, WU Ying-jie, ZHEN Cheng-gang. Rolling bearing fault diagnosis based on variational mode decomposition and fuzzy C means clustering[J]. **Proceedings of the CSEE**, 2015, 35(13): 3358−3365.

[9] REN H, LIU W Y, SHAN M C, et al. A new wind turbine health condition monitoring method based on VMD-MPE and feature-based transfer learning[J]. **Measurement**, 2019, 148: 106906.

[10] CAI G W, WANG L X, YANG D Y, et al. Harmonic detection for power grids using adaptive variational mode decomposition[J]. **Energies**, 2019, 12(2): 1−16.

[11] LIAN J J, LIU Z, WANG H J, et al. Adaptive variational mode decomposition method for signal processing based on mode characteristic[J]. **Mechanical Systems and Signal Processing**, 2018, 107: 53−77.

[12] GU R, CHEN J, HONG R J, et al. Incipient fault diagnosis of rolling bearings based on adaptive variational mode decomposition and Teager energy operator[J]. **Measurement**, 2020, 149: 106941.

[13] ZHANG Xin, MIAO Qiang, ZHANG Heng, et al. A parameter-adaptive VMD method based on grasshopper optimization algorithm to analyze vibration signals from rotating machinery[J]. **Mechanical Systems and Signal Processing**, 2018, 108: 58−72.

[14] YANG K, WANG G F, DONG Y, et al. Early chatter identification based on an optimized variational mode decomposition[J]. **Mechanical Systems and Signal Processing**, 2019, 115: 238−254.

[15] JIA Bao-xin, ZHOU Lin-li. An improved microseismic wave propagation velocity model for layered media in the goaf subsidence area[J]. **Journal of China University of Mining & Technology**, 2022, 51(4):673−688.

[16] JIA Bao-xin, CHEN Hao, WANG Kun, et al. Experimental study of microseismic propagation of layered rock mass with special geological structure[J]. **Rock and Soil Mechanics**, 2023, 44(1): 54−66.

[17] ZHAO Yang-feng, JING Gang, CHENG Chuan-jie, et al. Tests for fracture characteristics of fractured sandstone and micro-seismic and charge induced signal laws[J]. **Journal of Vibration and Shock**, 2020, 39(23): 211−219, 233.

[18] MARTíNEZ-MARTíNEZ J, BENAVENTE D, GARCíA-DEL-CURA MA. Spatial attenuation: the most sensitive ultrasonic parameter for detecting petrographic features and decay processes in carbonate rocks[J]. **Engineering Geology**, 2011, 119(3−4): 84−95.

[19] LIU Fei. Study on the evolution and warning of rockbursts in deep-buried tunnels of the Hanjiang-to-Weihe River diversion project by microseismic monitoring[D] Dalian: Dalian University of Technology, 2020.

[20] LIU Yao-qi, CAO An-ye, WANG Song-wei, et al. Prediction method of coal burst based on attenuation characteristics of seismic cluster energy[J]. **Journal of China Coal Society**, 2022, 47(4): 1523−1533.

[21] LIU Hai-shun, JING Guang-cheng, XIE Long, et al. Variation of microseismic signal with energy: a case study of Zhangxiaolou coal mine[J]. **Journal of Mining & Safety Engineering**, 2018, 35(2): 316−323.

[22] JING Lin-bo. Study on mine microseismic signal characteristics and propagation law[D] Xuzhou: China University of Mining and Technology, 2014.

[23] ZHANG X L, JIA R S, LU X M, et al. Identification of blasting vibration and coal-rock fracturing microseismic signals[J]. **Applied Geophysics**, 2018, 15(2): 280−289.

[24] ZHOU L L, JIA B X, ZHENG K N, et al. Energy and frequency characteristics of microseismic particles in a complex geological model[J]. **Advanced Theory and Simulations**, 2022, 5(12): 2200576.

[25] JIA Bao-xin, CHEN Hao, WANG Kun, et al. Experimental study of microseismic propagation of layered rock mass with special geological structure[J]. **Rock and Soil Mechanics,** 2023, 44(1): 54−66.

[26] LI Zhi-yong. Study on the deformation rule of roadway surrounding rock under the condition of stubble mining[D] Fuxin: Liaoning Technical University, 2020.

[27] CAI M, KAISER P K, MORIOKA H, et al. FLAC/PFC coupled numerical simulation of AE in large-scale underground excavations[J]. **International Journal of Rock Mechanics and Mining Sciences**, 2007, 44(4): 550−564.